

NUMERICAL METHODS FOR MULTISCALE INVERSE PROBLEMS *

CHRISTINA FREDERICK [†] AND BJÖRN ENGQUIST [‡]

Abstract. We consider the inverse problem of determining the highly oscillatory coefficient a^ϵ in partial differential equations of the form $-\nabla \cdot (a^\epsilon \nabla u^\epsilon) + bu^\epsilon = f$ from given measurements of the solutions. Here, ϵ indicates the smallest characteristic wavelength in the problem ($0 < \epsilon \ll 1$). In addition to the general difficulty of finding an inverse, the oscillatory nature of the forward problem creates an additional challenge of multiscale modeling, which is hard even for forward computations. The inverse problem in its full generality is typically ill-posed and one common approach is to replace the original problem with an effective parameter estimation problem. We will here include microscale features directly in the inverse problem and avoid ill-posedness by assuming that the microscale can be accurately represented by a low-dimensional parametrization. The basis for our inversion will be a coupling of the parametrization to analytic homogenization or a coupling to efficient multiscale numerical methods when analytic homogenization is not available. We will analyze the reduced problem, $b=0$, by proving uniqueness of the inverse in certain problem classes and by numerical examples and also include numerical model examples for medical imaging, $b>0$, and exploration seismology, $b<0$.

1. Introduction

This paper focuses on developing mathematical and numerical models used in the recovery of high resolution information about physical processes from observational data. A major hurdle in these problems is the high computational cost associated with the forward simulations, especially when the models contain variations on a wide range of scales. The main contribution of this paper is the application of multiscale techniques for highly oscillatory models that results in well-posed inverse problems that can be implemented efficiently. An application is medical imaging, where reconstructions are obtained from experiments that use photo-acoustic effects of optical and ultrasonic waves [4, 5]. Multiscale modeling also plays a key role in reflection seismology [24], where accurate models of seismic wave propagation in the Earth's sedimentary crust must account for a wide spectrum of time and spatial scales.

Of present interest are inverse problems for determining an unknown parameter in a forward model $G: X \rightarrow P$, where G is often a solution operator for a partial differential equation, and X and P are function spaces. In particular, we consider models of physical processes that contain variations on multiple scales. Such processes are governed by partial differential equations of the form $G(a^\epsilon) = u^\epsilon \in P$, where the parameter $a^\epsilon \in X$ is a coefficient in the equation. The multiscale nature of the problem is indicated by the superscript ϵ , where ϵ is the ratio of scales in the model ($0 < \epsilon \ll 1$).

The collected measurements, denoted by $y^\epsilon \in \mathbb{R}^n$, are in practice obtained from experiments or electrical techniques. In the current framework, the mapping from the unknown parameter to the data is derived using the forward model. This mapping is called the *observation operator*, and is denoted by $\mathcal{G}: X \times P \rightarrow \mathbb{R}^n$. The solution to the inverse problem is then obtained by matching observations $y^\epsilon = \mathcal{G}(a^\epsilon, u^\epsilon)$, with predictions of the form $z = \mathcal{G}(\hat{a}^\epsilon, \hat{u}^\epsilon)$. In practice, the mapping from the parameter space to the space of predictions may differ from the observation operator, however here it is assumed that the mappings are the same.

*Received date / Revised version date

[†]School of Mathematics, Georgia Institute of Technology, Atlanta, GA, 30332, USA (cfrederick6@math.gatech.edu).

[‡]Institute for Engineering and Scientific Computing (ICES) and Department of Mathematics at The University of Texas at Austin, Austin, TX 78712, USA (engquist@ices.utexas.edu).

Data-driven optimization problems require many simulations of the forward model, and when faced with balancing computational cost with accuracy, most approaches only deal with scientific models of large scale behavior and, for example in [20], account for microscopic processes by using effective or homogenized equations to simplify computations. Homogenization theory [6, 15] provides the form of a reduced model that describes the effective behavior of the family of solutions $\{G(a^\epsilon)\}_{\epsilon>0}$; under certain ellipticity conditions, it is known that $G(a^\epsilon) \rightharpoonup U$, as $\epsilon \rightarrow 0$, where U is the solution to an equation of the form $G(A) = U$, and the expression for A is given by the theory. Here, A is called an *effective* or *homogenized* coefficient corresponding to a^ϵ .

Ideas from homogenization theory can be used to account for the mismatch in scales between an effective model and the data generated by the full model, as demonstrated in [20]. The authors show that if only effective parameters in the forward model are desired, inversion can be performed using macroscopic predictions. In particular, the result is shown for cases where unknown coefficient A is dependent on a single scalar parameter $\theta \in \mathbb{R}$ through a linear mapping $\theta \rightarrow A(\theta)$. The inverse problem is formulated as a minimization problem,

$$\underset{\theta \in \mathbb{R}, A=A(\theta)}{\text{minimize}} \quad \|\mathcal{G}(A, G(A)) - y^\epsilon\|. \quad (\text{IP}^0)$$

The benefits of the reduced formulation (1.1) include well-posedness and a lowered sensitivity to noise in the reconstruction. A drawback of this approach is the loss of details about microscale features due to the reduced parameter space.

In the current approach, full inversion is performed using effective forward models that are based on ideas from homogenization theory, as in [20]. The increased resolution of the recovered parameter is a result of the assumption of a *microscale* parametrization

$$m(x) \rightarrow a^\epsilon(m(x)),$$

where m lies in an infinite dimensional function space and is independent of ϵ . Non-linear mappings $m \rightarrow a^\epsilon(m)$ are allowed in this formulation.

Then, macroscopic predictions are made using ideas from homogenization theory, gaining the benefits of the previous approach,

$$\underset{m, a^\epsilon=a^\epsilon(m)}{\text{minimize}} \quad \|\mathcal{G}(a^\epsilon, G(A)) - y^\epsilon\|. \quad (\text{IP})$$

We will give sufficient conditions for well-posedness of the continuous inverse problem for partial differential equations that is related to (IP). These conditions correspond to a classification of certain physical features of the microstructure that are preserved under homogenization.

The following is a summary of numerical approaches for inverse problems for multiscale model parameters.

- I. **Full coefficient inversion.** Full coefficient inversion is performed by minimizing the distance between model predictions and the given data,

$$\underset{a^\epsilon}{\text{minimize}} \quad \|\mathcal{G}(a^\epsilon, G(a^\epsilon)) - y^\epsilon\|. \quad (\text{IP}^\epsilon)$$

Determining the original coefficient using high resolution predictions comes at a large computational cost and is often ill-posed due to the presence of multiple local minima in the associated cost functionals. Therefore, we omit this case from our computations.

II. Indirect microscale parameter estimation. An indirect method for solving (IP) involves a two-stage procedure. The first step is to solve the problem of estimating the parameter \hat{A} in the effective model that best matches the given data. The second step involves determining the microscale parameter m such that the homogenization of $a^\epsilon(m)$ is \hat{A} . This method can be written as

- i. minimize $\|\mathcal{G}(A, G(A)) - y^\epsilon\| \rightarrow \hat{A}$
- ii. minimize $\|A(m) - \hat{A}\|$.

III. Direct microscale parameter estimation.

In this case, (IP) is solved in one step, where predictions of the forward model are made using techniques from multiscale modeling and numerical homogenization. In our experiments we consider two methods.

- a. *Known homogenization.* If the explicit form of the homogenized coefficient corresponding to each parameter $m \rightarrow a^\epsilon(m) \rightarrow A(m)$ is known, a macroscopic method can be used to solve the effective equation.

$$\underset{m \in X, A=A(m)}{\text{minimize}} \quad \|\mathcal{G}(A, G(A)) - y^\epsilon\|. \quad (1.1)$$

- b. *HMM.* Often, the explicit form of the homogenized coefficient is not available, preventing the direct computation of macroscopic predictions. This issue can be overcome numerically with the heterogeneous multiscale method, or HMM, introduced by E and Engquist [10]. HMM provides a framework for the design of methods that capture macroscale properties of a system using microscale information. The inverse problem is formulated as

$$\underset{m, a^\epsilon=a^\epsilon(m)}{\text{minimize}} \quad \|\mathcal{G}(a^\epsilon, G(A)) - y^\epsilon\|. \quad (1.2)$$

Here, the forward model $G(A)$ is approximated using methods for numerical homogenization of the predicted coefficient a^ϵ . In the experiments we use the heterogeneous multiscale method (HMM).

The paper is organized as follows. We present results from homogenization theory in §2. For the analysis in §3, we will introduce a multiscale inverse problem related to (IP) in the classical setting of inverse problems for elliptic equations and give sufficient conditions for well-posedness. In §6 we describe our implementation of the finite element heterogeneous multiscale method. Numerical results are provided in §8. In sections §8.2 and §8.3 we consider model problems from applications in medical imaging and geophysics. Then we conclude in §9.

1.1. Notation

The averaging operator is denoted by $\langle f \rangle_X = \frac{1}{|X|} \int_X f(y) dy$, where $|X|$ is the volume of the set $X \subset \mathbb{R}^d$. For most examples $Y = [0, 1]^d$, and unless otherwise stated, $\langle \cdot \rangle = \langle \cdot \rangle_Y$. For any domain D , we use the Sobolev space $W^{m,p}(D)$ with Sobolev norm $\|\cdot\|_{W^{m,p}}$. If $D = \Omega$, we omit D . Moreover, if $D = \Omega$ and $p = 2$, we denote by $H^m(\Omega)$ the Sobolev space $W^{m,2}(\Omega)$, the usual L^2 inner product by (\cdot, \cdot) and the Sobolev norm by $\|\cdot\|_m$.

2. Deriving effective forward models Let $\Omega \subset \mathbb{R}^d$ be a bounded domain. We consider equations for which there is a well established homogenization theory,

$$-\nabla \cdot (a^\epsilon \nabla u^\epsilon) + b u^\epsilon = f \text{ in } \Omega, \quad (2.1)$$

where f and b are given bounded functions. The unknown coefficient is given by $a^\epsilon(x) = a(x, x/\epsilon)$ for a given matrix function a that is locally-periodic, symmetric, and uniformly positive definite. Equations of the form (2.1) govern the physics of heterogeneous materials, and the full recovery of these coefficients gives detailed information about the microstructure.

Homogenization theory provides an effective model that describes the limiting behavior of solutions to (2.1) [6, 15]. A constant positive definite matrix A is said to be the homogenized matrix for a , if for any bounded domain $D \subset \mathbb{R}^d$ and any $f \in H^{-1}(D)$ the solutions of the Dirichlet problem (2.1) possess the following property of convergence: as $\epsilon \rightarrow 0$, $u^\epsilon \rightharpoonup U$ weakly in H_0^1 and $a^\epsilon \nabla u^\epsilon \rightarrow A \nabla U$ strongly in L_2 , where U is the solution of the Dirichlet problem

$$-\operatorname{div}(A(x) \nabla U(x)) + bU = f \text{ in } \Omega. \quad (2.2)$$

The homogenized coefficient has a closed form,

$$A(x) = \frac{1}{|Y|} \int_Y (a(x, y) Id + a(x, y) \nabla_y \chi) dy, \quad (2.3)$$

where $\chi = (\chi_1, \chi_2)$ solves the cell problems:

$$-\nabla_y \cdot (a(x, y) \nabla_y \chi) = \nabla_y \cdot a(x, y) Id \quad (2.4)$$

with the constraint $\chi(x, y)$ is Y -periodic in y and $\langle \chi(x, \cdot) \rangle = 0$.

The theory of homogenization will be used to predict the effective behavior of oscillatory solutions to the original model. In the next section we will examine the relationship between the highly oscillatory coefficients in the full equation (2.1) and the homogenized model (2.2).

3. Multiscale analysis for the inverse conductivity problem The goal of this section is to derive an effective model corresponding to the multiscale forward model. Let Ω be an open, bounded region in \mathbb{R}^d , $d \geq 2$, that has a sufficiently smooth boundary $\partial\Omega$. In applications [23, 25], Ω is thought of as a conducting medium with spatially varying electrical properties. The steady state voltage potential u satisfies the Dirichlet problem

$$-\operatorname{div}(A \nabla u) = 0 \text{ in } \Omega. \quad (3.1)$$

The coefficient A , referred to as the conductivity, is in general a uniformly positive definite, symmetric, $d \times d$ matrix; if A is scalar we say that the conductivity is isotropic, in all other cases it is called anisotropic [25]. The aim of inverse conductivity problems is to determine the conductivity using data from multiple boundary measurements.

DEFINITION 3.1. For $g, h \in H^{1/2}(\partial\Omega)$ let $u \in H^1(\Omega)$ be the weak solution to (3.1) subject to $u|_{\partial\Omega} = g$, and let g be an arbitrary function in $H^1(\Omega)$ that satisfies $v|_{\partial\Omega} = h$. The Dirichlet-to-Neumann map $\Lambda_A : H^{1/2}(\partial\Omega) \rightarrow H^{-1/2}(\partial\Omega)$ is defined by

$$\langle \Lambda_A g, h \rangle = \int_{\Omega} A(x) \nabla u(x) \cdot \nabla v(x) dx. \quad (3.2)$$

The inverse boundary value problem of Calderón [8], also known as the inverse conductivity problem or electrical impedance tomography, is to recover A from knowledge of the Dirichlet-to-Neumann map Λ_A . For recent results involving uniqueness

and reconstruction, see [7, 9, 26]. In order to resolve stability issues (described in [1]), some approaches replace a-priori regularity assumptions for A with different assumptions that are better suited for applications.

For general anisotropic conductivities, the inverse conductivity problem does not admit a unique solution. However, in [2], uniqueness of the inverse problem is proved in cases where there is prior knowledge of a parametrization

$$m(x) \rightarrow A(m(x), x) \quad (3.3)$$

for a bounded, scalar function m . A key assumption is that the matrix-valued function A possesses special anisotropy, defined in terms of properties of the derivative $D_m A$.

DEFINITION 3.2 (Adapted from Definition 2.2 in [2]). *Given $p > d$, $E > 0$, and denoting by Sym_d the class of $d \times d$ real-valued symmetric matrices, we say $A(\cdot, \cdot) \in \mathcal{H}$ if the following conditions are satisfied:*

$$\begin{aligned} A &\in W^{1,p}([\lambda^{-1}, \lambda] \times \Omega, Sym_d), \\ D_m A &\in W^{1,p}([\lambda^{-1}, \lambda] \times \Omega), \\ \sup_{m \in [\lambda^{-1}, \lambda]} &(\|A(m, \cdot)\|_{L^p(\Omega)} + \|D_x A(m, \cdot)\|_{L^p(\Omega)}, \\ &+ \|D_m A(m, \cdot)\|_{L^p(\Omega)} + \|D_m D_x A(m, \cdot)\|_{L^p(\Omega)}) \leq E, \\ \lambda^{-1}|\xi|^2 &\leq A(m, x)\xi \cdot \xi \leq \lambda|\xi|^2 \text{ for a.e. } x \in \Omega \text{ and all } m \in [\lambda^{-1}, \lambda], \xi \in \mathbb{R}^d. \end{aligned}$$

In addition, the following monotonicity condition must also be satisfied:

$$D_m A(m, x)\xi \cdot \xi \geq E^{-1}|\xi|^2 \quad (3.4)$$

for a.e. $x \in \Omega$ and all $m \in [\lambda^{-1}, \lambda], \xi \in \mathbb{R}^d$.

The following theorem, adapted to our context, is from [2]. It gives a global uniqueness result for matrices $A(\cdot, \cdot) \in \mathcal{H}$.

THEOREM 4 (Adapted from Theorem 2.1 in Alessandrini, Gaburro, 2001). *Given $p > d$, let Ω be a bounded Lipschitz domain with constants L, r, h . Let m_1, m_2 satisfy*

$$\lambda^{-1} \leq m_1(x), m_2(x) \leq \lambda \text{ for all } x \in \Omega, \quad (4.1)$$

$$\|m_1\|_{W^{1,p}(\Omega)}, \|m_2\|_{W^{1,p}(\Omega)} \leq E. \quad (4.2)$$

Let A be sufficiently bounded and monotone; then,

$$\|A(m_1(x), x) - A(m_2(x), x)\|_{L^\infty(\partial\Omega)} \leq C \|\Lambda_{A(m_1(x), x)} - \Lambda_{A(m_2(x), x)}\|_*.$$

Here C is a constant that depends only on $d, p, L, r, \text{diam}(\Omega), \lambda$ and E .

THEOREM 5 (Adapted from Theorem 2.4 in Alessandrini, Gaburro, 2001). *Suppose m_1, m_2 satisfy (4.1) and (4.2). Suppose also that Ω can be partitioned into a finite number of domains $\{\Omega_j\}_{j \leq N}$, with $m_1 - m_2$ analytic on each $\overline{\Omega_j}$. Then, $\Lambda_{A(m_2, \cdot)} = \Lambda_{A(m_1, \cdot)}$ implies that $A(m_1, \cdot) = A(m_2, \cdot)$ in Ω .*

This result gives sufficient conditions on the parameterization $m \rightarrow A(m)$ that guarantee the unique recovery of A from the Dirichlet-to-Neumann map Λ_A . We extend this theory to the multiscale inverse problem of determining a^ϵ using macroscopic data Λ_A by adding assumptions about the monotonicity of the parametrization of the multiscale coefficient a^ϵ . In particular, the following result holds.

THEOREM 5.1. *Suppose that $a(\cdot, \cdot)$ is a $d \times d$, symmetric matrix function that is locally-periodic, symmetric, and uniformly positive definite and Lipschitz in the first*

variable. Furthermore, suppose $a(\cdot, \cdot)$ admits a homogenized coefficient $A \in \mathcal{H}$. Let m_1 and m_2 be functions that satisfy (4.1) and (4.2) and suppose the difference $m_1 - m_2$ is piecewise analytic on Ω . Then, for $\epsilon > 0$ and $i = 1, 2$, defining $a_i^\epsilon = a(m_i(x), x/\epsilon)$, $A_i = A(m_i(x), x)$, it follows that $\Lambda_{A_1} = \Lambda_{A_2}$ implies that $a_1^\epsilon = a_2^\epsilon$ in Ω . Furthermore, there is a constant $C > 0$ with

$$\|a_1^\epsilon - a_2^\epsilon\|_{L^\infty(\partial\Omega)} \leq C \|\Lambda_{A_1} - \Lambda_{A_2}\|_* \quad (5.1)$$

Proof. A part of the proof of Theorem 5 in [2] involves showing that for $A \in \mathcal{H}$ there exists a positive constant C_1 with $\|m_1 - m_2\| \leq C_1 \|\Lambda_{A(m_1(x), x)} - \Lambda_{A(m_2(x), x)}\|_*$. The Lipschitz continuity of a gives the stability result,

$$\|a(m_1, \cdot) - a(m_2, \cdot)\|_{L^\infty(\partial\Omega)} \leq K \|m_1 - m_2\| \leq C \|\Lambda_{A(m_1(x), x)} - \Lambda_{A(m_2(x), x)}\|_*.$$

□

In the next sections we will describe key models for microstructure that we use in the numerical experiments to demonstrate (5.1).

5.1. Determining anisotropy of effective coefficients

Let $\Omega \in \mathbb{R}^2$ be a bounded, measurable domain and let $m(x)$ be a scalar function taking values in the interval $I_\lambda = [\lambda^{-1}, 1]$. The coefficients in the equation (2.1) represent properties of heterogeneous, isotropic materials,

$$a^\epsilon(x) = a(m(x), x/\epsilon) Id, \quad (5.2)$$

where $a(x, y)$ is a bounded, locally-periodic function with $a(x, y) > a_* > 0$ for some constant a_* . Explicit solutions of the corresponding homogenized coefficients can be found in the case $d=1$, and also in certain higher dimensional models that have a one-dimensional character, such as those describing layered media [15].

The first three cases are commonly used models of layered materials (see Figure 5.1). The last two models represent properties of materials containing cell microstructures (see Figure 5.2).

A. **Amplitude.** For a positive constant a_0 and a periodic function $\bar{a} \in L_\infty(\Omega)$ with $\langle \bar{a} \rangle = 0$, the parametrization of the amplitude of oscillations is modeled by

$$a(m, y) = a_0 + m\bar{a}(y_2), \quad (5.3)$$

B. **Area fraction.** A special case of layered materials are two-phase laminates, where the parameter m determines the volume fraction of each constituent,

$$a(m, y) = \begin{cases} k_1 & 0 \leq y_2 < m \\ k_2 & m \leq y_2 < 1. \end{cases} \quad (5.4)$$

C. **Angle.** Here, \hat{a} is a periodic function and σ_m is a matrix of rotation,

$$a(m, y) = \hat{a}(\sigma_m y), \quad \sigma_m = \begin{pmatrix} \cos 2\pi m & \sin 2\pi m \\ -\sin 2\pi m & \cos 2\pi m \end{pmatrix}. \quad (5.5)$$

D. **Amplitude in cell structures.** The analog of ModelA is a class of separable functions a ,

$$a(m, y) = a_1(m, y_1) a_2(m, y_2), \quad (5.6)$$

where a_1 and a_2 of the type in (5.3).

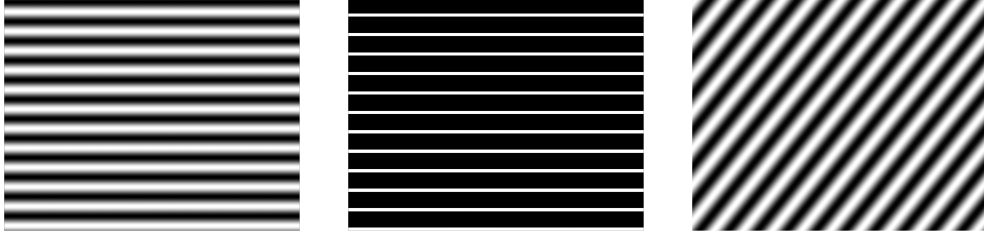


FIG. 5.1. **Layered microstructure.** From left to right: A - Amplitude, B - Area fraction, C - Angle.

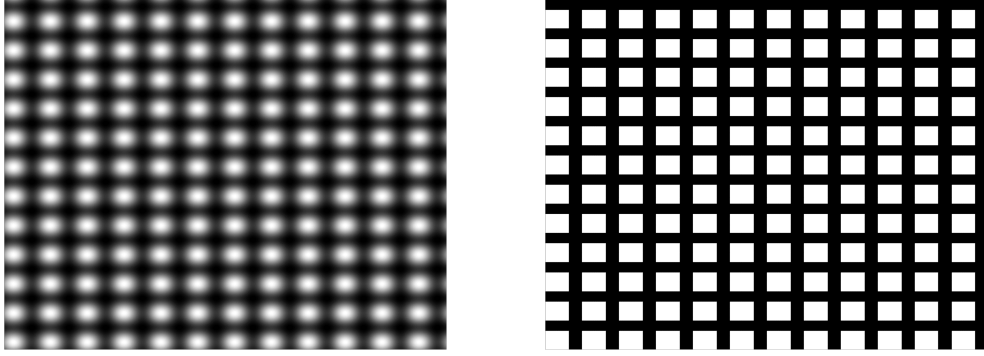


FIG. 5.2. **Cell microstructures.** Piecewise constant functions are used to model cell structures (left) D - Amplitude and (right) E - Area Fraction.

E. Area fraction in cell structures. The analog of Model B is modeled by

$$a(m, y) = \begin{cases} k_1 & y \in mY \\ k_2 & \text{otherwise.} \end{cases} \quad (5.7)$$

5.1.1. Explicit calculations of the homogenized coefficient

For the calculations in this section we fix m to be a constant function in the interval $\lambda^{-1} \leq m \leq 1$. Since the models introduced in §5.1 are locally-periodic and isotropic, that is,

$$a^\epsilon = a(m(x), x/\epsilon) Id,$$

it follows that the homogenized coefficients are constant matrix functions,

$$A(m(x), x) = A(m).$$

In two dimensions, calculations of (2.3) can be made explicitly.

Layered materials. The microstructure contains oscillations in one direction, such as in the examples A and B. The homogenized coefficient is the diagonal matrix

$$A(m) = \begin{pmatrix} \langle a(m, \cdot) \rangle & 0 \\ 0 & \langle a(m, \cdot)^{-1} \rangle^{-1} \end{pmatrix}. \quad (5.8)$$

CALCULATION 1. Since $a = a(m, y_2)$, the cell problems (2.4) can be expressed as

$$\begin{aligned} -\frac{\partial}{\partial y_2}(a(m, y_2) \frac{\partial}{\partial y_2} \chi_1) &= 0, \\ -\frac{\partial}{\partial y_2}(a(m, y_2) \frac{\partial}{\partial y_2} \chi_2) &= \frac{\partial}{\partial y_2} a(m, y_2), \end{aligned}$$

where the solutions are of the form $\chi = (\chi_1(m, y_2), \chi_2(m, y_2))$. Integration from 0 to y_2 gives

$$a(m, y_2) \frac{\partial \chi_1}{\partial y_2} = c_1, \quad (5.9)$$

$$a(m, y_2) \frac{\partial \chi_2}{\partial y_2} = -a(m, y_2) + d_1, \quad (5.10)$$

for some constants $c_1(m), d_1(m)$. Since a is strictly positive, we can divide (5.9) and (5.10) by $a(m, y_2)$ and integrate from 0 to y_2 again

$$\chi_1 = c_1 \int_0^{y_2} \frac{1}{a(m, \xi)} d\xi + c_2, \quad \chi_2 = -y_2 + d_1 \int_0^{y_2} \frac{1}{a(m, \xi)} d\xi + d_2.$$

Now, using periodicity, $\chi_l(0, m) = \chi_l(1, m)$ it follows that $c_1 = 0$, and $d_1 = \langle a(m, \cdot)^{-1} \rangle^{-1}$. Therefore (5.9) and (5.10) become

$$\begin{aligned} a(m, y_2) \frac{\partial \chi_1}{\partial y_2} &= 0, \\ a(m, y_2) \frac{\partial \chi_2}{\partial y_2} &= -a(m, y_2) + \langle a(m, \cdot)^{-1} \rangle^{-1}. \end{aligned}$$

Substituting these expressions into (2.3) results in the explicit form of the homogenized coefficient.

Materials with oriented layers. Suppose a is of the form (5.5) with $\hat{a}(y) = \hat{a}(y_2)$ for all $y = (y_1, y_2)$. The homogenized coefficient is then

$$A(m) = \sigma_m^T \begin{pmatrix} \langle \hat{a} \rangle & 0 \\ 0 & \langle \hat{a}^{-1} \rangle^{-1} \end{pmatrix} \sigma_m. \quad (5.11)$$

CALCULATION 2. Let $\sigma = \sigma_m$. For a bounded set $\Omega \subset \mathbb{R}^2$, consider the scalar problems

$$\begin{aligned} \int_{\Omega} \nabla \psi \cdot \hat{a}(x/\epsilon) \nabla u^\epsilon dx &= 0, \quad \forall \psi \in H_0^1(\Omega) \quad \text{for } u^\epsilon \in H_0^1(\Omega), \\ \int_{\Omega} \nabla \psi \cdot \hat{A} \nabla U dx &= 0, \quad \forall \psi \in H_0^1(\Omega) \quad \text{for } U \in H_0^1(\Omega). \end{aligned}$$

Now consider the change of variables $x = \sigma y$ where σ is an orthogonal transformation from \mathbb{R}^2 to \mathbb{R}^2 . We obtain the Dirichlet problems for $\Omega' = \sigma^{-1}\Omega$,

$$\begin{aligned} \int_{\Omega'} \nabla_y \psi \cdot \hat{a}(\sigma y/\epsilon) \nabla_y u^\epsilon(\sigma y) dy &= 0, \\ \int_{\Omega'} \nabla_y \psi \cdot \sigma \hat{A} \sigma^{-1} \nabla_y U(\sigma y) dy &= 0. \end{aligned}$$

Since $u^\epsilon(\sigma y) \rightharpoonup U(\sigma y)$ in $H_0^1(\Omega')$, it follows that the homogenized coefficient corresponding to (5.5) is $\sigma \hat{A} \sigma^{-1}$.

Homogenization of cell structures. It is well known [15, 19] that the homogenized coefficient corresponding a separable function of the form (5.6) is the diagonal matrix

$$A(m) = a_0 \begin{pmatrix} \langle a_1(m, \cdot)^{-1} \rangle^{-1} & 0 \\ 0 & \langle a_2(m, \cdot)^{-1} \rangle^{-1} \end{pmatrix}. \quad (5.12)$$

In addition, homogenization formulas for functions of the form (5.7) can be derived explicitly,

$$A(m) = \bar{a}(m) Id, \quad (5.13)$$

$$\bar{a}(m) = \int_0^1 \left(\int_0^1 \frac{1}{a(m, y)} dy_1 \right)^{-1} dy_2. \quad (5.14)$$

CALCULATION 3. *The homogenized coefficient corresponding to $a(m, y)$ is given by*

$$A(m) = \frac{1}{|Y|} \int_Y (a(m, y) Id + a(m, y) \nabla_y \chi) dy, \quad (5.15)$$

where $\chi = (\chi_1, \chi_2)$ solves the cell problems

$$-\nabla_y \cdot (a(m, y) \nabla_y \chi) = \nabla_y \cdot a(m, y) Id, \quad (5.16)$$

with the constraint $\chi_i(m, y)$ is Y -periodic in y and

$$\int_Y \chi_i(m, y) dy = 0.$$

The solutions to the cell problems (5.16) are equivalent to

$$\begin{aligned} \frac{\partial}{\partial y_i} \left(a(m, y) \frac{\partial \chi_k}{\partial y_i} \right) &= -\frac{\partial}{\partial y_i} a(m, y), & i=1, 2, \quad k=i, \\ \frac{\partial}{\partial y_i} \left(a(m, y) \frac{\partial \chi_k}{\partial y_i} \right) &= 0, & i=1, 2, \quad k \neq i. \end{aligned} \quad (5.17)$$

Furthermore, the function $a(m, y)$ satisfies the condition of cubic symmetry (see [15]), and therefore the homogenized coefficient is isotropic; that is, (5.13) holds for a function \bar{a} to be determined. As a consequence, \bar{a} can be calculated using only the solution to (5.17) for $i=k=1$. Integration from 0 to y_1 gives

$$a(m, y) \frac{\partial \chi_1}{\partial y_1} = -a(m, y) + c_1, \quad (5.18)$$

where c_1 is a function of only m and y_2 . Since a is positive, we can divide by a and integrate from 0 to y_1 again, giving

$$\chi_1 = -y_1 + c_1 \int_0^{y_1} \frac{1}{a(m, y)} dy_1 + c_2,$$

where c_2 is also a function of only m and y_2 . Applying the periodic boundary conditions $\chi_1|_{y_1=0} = \chi_1|_{y_1=1}$ results in

$$c_1(m, y_2) = \left(\int_0^1 \frac{1}{a(m, y)} dy_1 \right)^{-1}.$$

Therefore (5.18) becomes

$$a(m, y) \frac{\partial}{\partial y_1} \chi_1 = -a(m, y) + \left(\int_0^1 \frac{1}{a(m, y)} dy_1 \right)^{-1}.$$

Substituting these expressions into (5.15) results in the closed form for the homogenized coefficient (5.14).

5.2. Sufficient conditions for microscale recovery

In order to verify the assumptions needed for the stability result (5.1), the first step is to show that the coefficient a^ϵ must admit a homogenized matrix A that is a symmetric, uniformly positive definite matrix function with bounded elements. These conditions are automatically satisfied for a^ϵ defined by (5.2) and the models in the previous section.

The crucial step is to show that $A(m)$ is monotone in the sense of (3.4). The following calculations give conditions on the microstructure that guarantee this monotonicity.

The models A and B satisfy the monotonicity condition if there is a constant $E > 0$ with

$$D_m \langle a(m, \cdot)^{-1} \rangle^{-1} > E \text{ and } D_m \langle a(m, \cdot) \rangle > E.$$

In the model C, monotonicity condition is not satisfied; the matrix

$$D_m A = (\langle \hat{a}^{-1} \rangle^{-1} - \langle \hat{a} \rangle) \begin{pmatrix} -\sin 2m & \cos 2m \\ \cos 2m & \sin 2m \end{pmatrix}$$

has eigenvalues ± 1 . Therefore, Theorem 5 cannot be directly applied. In Section §8, we present numerical results for this case.

For the cell structure model D, monotonicity is satisfied if there is a constant $E > 0$ with

$$D_m \langle a_1(m, \cdot)^{-1} \rangle^{-1} > E \text{ and } D_m \langle a_2(m, \cdot)^{-1} \rangle^{-1} > E,$$

and for the last cell structure model E, the monotonicity requirement can be determined using the formula (5.14) for the isotropic homogenized coefficient.

CALCULATION 4. Defining the function $\varphi(m, y_2) = \int_0^1 \frac{1}{a(m, y)} dy_1$, it follows that

$$\begin{aligned} D_m \bar{a}(m) &= \int_0^1 \frac{\partial}{\partial m} [(\varphi(m, y_2))^{-1}] dy_2 \\ &= - \int_0^1 [(\varphi(m, y_2))^{-2}] \frac{\partial \varphi}{\partial m}(m, y) dy_2 \\ &= \int_0^1 \int_0^1 \frac{\frac{\partial a}{\partial m}(m, y)}{(\varphi(m, y_2) a(m, y))^2} dy_1 dy_2 \\ &\geq \lambda^{-4} \left\langle \frac{\partial a}{\partial m}(m, \cdot) \right\rangle. \end{aligned}$$

Therefore, the requirement that $\left\langle \frac{\partial a}{\partial m}(m, \cdot) \right\rangle > \lambda^4 E$ ensures that the monotonicity condition $D_m \bar{a}(m, y) > E > 0$ is satisfied for every $m \in I_\lambda$ and $y \in Y$.

REMARK 5.2. *It should be noted that these conditions are sufficient, but not necessary. In fact, an analogue of Theorem 5 holds in cases when the functions $D_m A$ is not strictly monotone.*

The specific models introduced here are chosen for two reasons. First, the models of amplitude and volume fraction give examples of conductivities that are continuously dependent on homogenized data according to (5.1). Second, all of the models give explicit homogenization formulas that can be used to derive forward solvers for the implementation of the inverse problem (IP). The forward solvers using the analytic formulas can then be compared with solvers using multiscale methods for numerical homogenization, described in the next section.

6. HMM for the forward problem

In the simulations, numerical homogenization is performed using the finite element heterogeneous multiscale method (FE-HMM). The macroscale bilinear form is defined for functions V and W lying in the finite element space X_H ,

$$\mathcal{B}(V, W) := \int_{\Omega} \nabla V \cdot A_{HMM}(x) \nabla W dx + \int_{\Omega} b W V dx, \quad (6.1)$$

where A_{HMM} is not known explicitly. The first integral in (6.1) is approximated using numerical quadrature points $\{x_l\}$ and weights $\{\omega_l\}$,

$$\mathcal{B}(V, W) \simeq \sum_{K \in \mathcal{T}_H} |K| \sum_{x_l \in K} \omega_l ((\nabla V \cdot A_{HMM} \nabla W)(x_l) + (b W V)(x_l)), \quad (6.2)$$

where $|K|$ is the measure of K .

A microscale solver is then used to estimate entries of the stiffness matrix. The effective behavior of a^ϵ is captured locally through the solution of cell problems

$$-\nabla \cdot (a^\epsilon \nabla v_l^\epsilon) = 0 \text{ in } I_\delta(x_l) := x_l \pm \frac{\delta}{2} I, \quad (6.3)$$

with the boundary condition $v_l^\epsilon = V_l$ on $\partial I_\delta(x_l)$, where V_l is the linear approximation of V at x_l . In our experiments, we set the microscale solver to be a \mathcal{P}_1 finite element method with triangulations \mathcal{T}_k^l of the subdomains $I_\delta(x_l)$. The spacing $k < \epsilon$ is chosen sufficiently small in order to resolve the microscale. Figure 6.1 contains a diagram of the macro-micro grid coupling in a typical FEM-HMM formulation.

Then, the term $(\nabla V \cdot A_{HMM} \nabla W)(x_l)$ in (6.2) can be estimated by

$$(\nabla V \cdot A_{HMM} \nabla W)(x_l) \simeq \frac{1}{\delta^n} \int_{I_\delta(x_l)} \nabla v_l^\epsilon \cdot (a^\epsilon \nabla w_l^\epsilon) dx.$$

The HMM bilinear form is then defined by

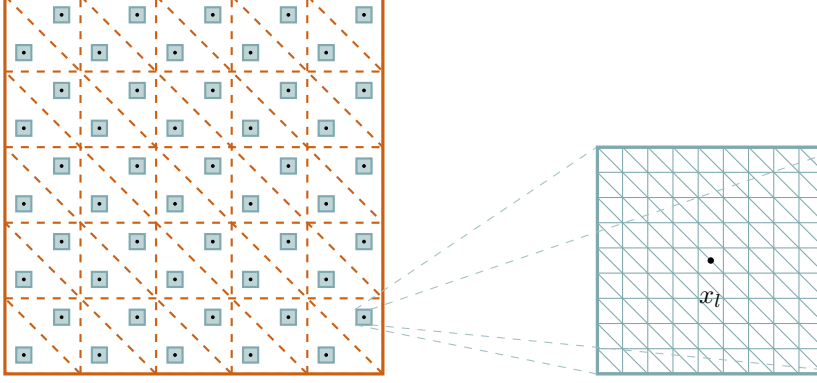
$$\mathcal{B}_{HMM}(V, W) := \sum_{K \in \mathcal{T}_H} \frac{|K|}{\delta^n} \sum_{x_l \in K} \omega_l \left(\int_{I_\delta(x_l)} \nabla v_l^\epsilon \cdot (a^\epsilon \nabla w_l^\epsilon) dx + (b W V)(x_l) \right).$$

Finally, we have that the HMM solution, $U_{HMM} \in g + X_H$, solves

$$\mathcal{B}_{HMM}(V, V) = (f, V),$$

for all $V \in X_H$.

FIG. 6.1. **FEM-HMM Discretization.** An illustration of coupled grids used in FE-HMM for elliptic PDEs. The orange dotted lines represent the macroscopic computational domain \mathcal{T}_H . The collection of light blue boxes represent the microscopic computational domains \mathcal{T}_k^l centered at the points x_l .



6.1. Errors in forward modeling

An analysis of the errors involved in the FE-HMM formulation for elliptic problems is found in [17]. The main result is the following theorem.

THEOREM 7 (Ming, Zhang 2005). *Denote by U, U_{HMM} the solutions to (2.2) and the FE-HMM solution, respectively. Let*

$$e(HMM) = \max_{x_l \in K, K \in \mathcal{T}_H} \|A(x_l) - A_{HMM}(x_l)\|,$$

where $\|\cdot\|$ is the Euclidean norm. If U is sufficiently smooth, and $\lambda I \leq a^\epsilon \leq \Lambda I$ for $\lambda, \Lambda > 0$, then there exists a constant C independent of ϵ, δ and H such that

$$\begin{aligned} \|U - U_{HMM}\|_1 &\leq C(H^k + e(HMM)), \\ \|U - U_{HMM}\|_0 &\leq C(H^{k+1} + e(HMM)). \end{aligned}$$

Then $U_{HMM} \rightarrow U$ as $e(HMM) \rightarrow 0$. For the periodic homogenization problem it is also shown that

$$e(HMM) \leq \begin{cases} C\epsilon & I_\delta(x_l) = x_l + \epsilon I \\ C(\frac{\epsilon}{\delta} + \delta) & \text{otherwise.} \end{cases}$$

The errors in our implementation of HMM are plotted in Figure 7.1 and Figure 7.2. The full solution to (2.1) with $f=1$ subject to Dirichlet boundary conditions $u^\epsilon|_{\partial\Omega}=0$ is computed using direct numerical simulation on a fine scale mesh with spacing $h=1/800$. Macroscopic solutions computed using analytic formulas and HMM, denoted by U_{HOM} and U_{HMM} respectively, are discretized on a coarse resolution mesh with spacing $H=1/20$. In the HMM simulations, local subdomains I_δ are used to approximate the effective coefficient. Figure 7.1 contains a plot of the errors between the oscillatory solution and the effective solutions as ϵ varies. In this case, a fixed HMM cell size $\delta=10\epsilon$ is used. Figure 7.2 contains a plot of the errors as the HMM cell size is varied and $\epsilon=1/100$.

FIG. 7.1. Error in macroscopic solution as $\epsilon \rightarrow 0$.

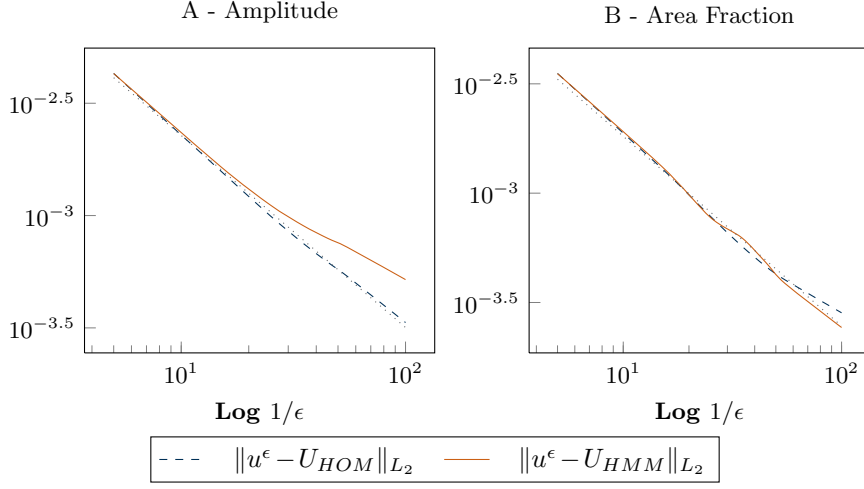
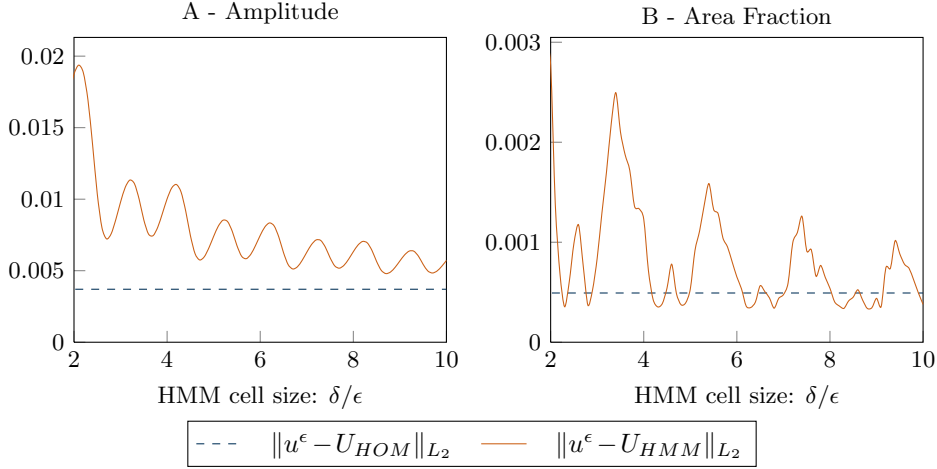


FIG. 7.2. Errors in macroscopic solution introduced by varying HMM cell size.



In the case of unknown or random microstructure, HMM can be performed “on the fly”, and computational time can be reduced using parallel solvers for the local cell problems. For periodic problems in two dimensions (as in this work), precomputing the cell problem solutions increases the efficiency of HMM.

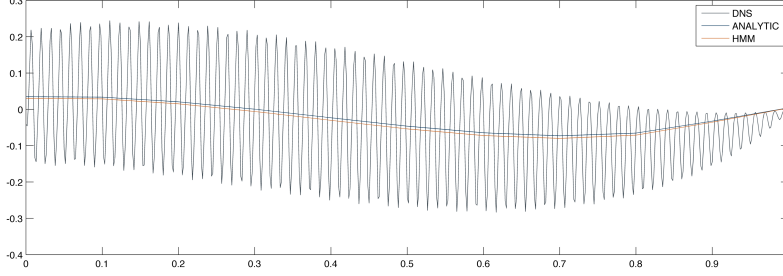
8. Numerical experiments

In this section we present results of numerical simulations that demonstrate parameter inversion of elliptic equations using homogenization theory and the ideas discussed in §3.

It is assumed that the parameter ϵ , as well as the mapping $m \rightarrow a^\epsilon(m)$ is known, and the inverse problem (IP) is solved by minimizing the cost functional

$$\Phi(m) = \|\mathcal{G}(A(m), G(A(m))) - y^\epsilon\|_2^2. \quad (8.1)$$

FIG. 8.1. **Synthetic data and predictions.** In the plot below, the black line is the Neumann data $\mathcal{G}(a^\epsilon) = a^\epsilon \nabla u^\epsilon \cdot n$ on the boundary segment $\Gamma = \{0 \leq x \leq 1, y = 0\}$ corresponding to the Dirichlet boundary condition $u|_{\partial\Omega} = \frac{1}{\sqrt{2\pi}} e^{-(x-1)^2}$, where a^ϵ is given by (5.5). The corresponding macroscopic predictions $\mathcal{G}(A) = A \nabla U \cdot n$ are also plotted.



In order to understand the effects of the regularization of the problem through the parameterization of the search space, we do not include additional regularization of the problem.

For the discrete problem, m is a scalar function with N degrees of freedom. We consider piecewise constant functions and spline interpolation between the values in a finite dimensional vector of unknowns, $\theta \in \mathbb{R}^N$. Later, we also show results of simulations where $m(x)$ is a vector-valued function that represents a parametrization of multiple microscale features.

An important consideration in addressing the mismatch in scales between the macroscopic predictions and data is that the observation operators must be designed to satisfy the following property,

$$\lim_{\epsilon \rightarrow 0} |\mathcal{G}(A, U) - \mathcal{G}(a^\epsilon, u^\epsilon)| = 0, \quad (8.2)$$

where A is the homogenized coefficient corresponding to a^ϵ . The justification here is based on the theory of homogenization and the convergence theory for HMM.

In all of the simulations, a standard \mathcal{P}^1 finite element method is used on a regular triangulation of the domain. The MATLAB routine `lsqnonlin` is used to minimize the least-squares functional (8.1). The synthetic data is generated using direct numerical simulation of the full model using a fine mesh with resolution $h < \epsilon$. Macroscopic predictions of the forward model are computed using a coarse mesh with resolution $H > \epsilon$. The local subdomains in the HMM solver are discretized on a fine mesh with spacing $\delta_x < \epsilon$. This provides a framework for microscale inversion that avoids the major pitfalls of committing an “inverse crime”. Unless otherwise stated, we set $\Omega = [0, 1] \times [0, 1]$, $\epsilon = 1/80$, $H = 1/10$, $\delta = 3\epsilon$, and $h = 1/600$.

8.1. Inverse conductivity ($\mathbf{b} = \mathbf{0}$) The ideas in §3 motivate the design observation operators $\mathcal{G}: X \rightarrow \mathbb{R}^n$ that satisfy (8.2). Based on the following convergence result from homogenization theory,

$$\lim_{\epsilon \rightarrow 0} \|A \nabla U - a^\epsilon \nabla u^\epsilon\|_{L^2} = 0, \quad (8.3)$$

we can justify the claim that $\mathcal{G}(a^\epsilon) \sim \mathcal{G}(A)$, where a^ϵ is an oscillatory function and A is the homogenized coefficient and \mathcal{G} is an approximation of the Dirichlet-to-Neumann

map,

$$\mathcal{G}(a)_k = a \nabla u_k \cdot n|_{\partial\Omega}$$

corresponding to solutions of for a discrete set of Dirichlet boundary conditions, $\{g_k\}$.

The microstructure in models A, B, and C, respectively, are represented by the coefficients

$$a_A^\epsilon(m(x), x) = 1.1 + m(x) \sin(2\pi x_2/\epsilon), \quad (8.4)$$

$$a_B^\epsilon(m(x), x) = .5 + 2\chi_{\{x_2 < m\}}(x), \quad (8.5)$$

$$a_C^\epsilon(m(x), x) = 1.1 + \sin(2\pi \tilde{x}_2/\epsilon), \quad \tilde{x} = \sigma_m x. \quad (8.6)$$

Figure 8.1 shows a plot of the Neumann data $\mathcal{G}(a^\epsilon) = a^\epsilon \nabla u^\epsilon \cdot n$ on a subset of the boundary $\partial\Omega$ and the macroscopic predictions using an analytic solver and HMM.

In the numerical simulations, we attempt to fit a homogenized model to the data by minimizing the functional (8.1). Forward predictions are made using an analytic solver, HMM, and a two-stage process for generating predictions. The differences in the inversion results can be attributed to the resolution of the meshes used, errors introduced by the optimization routine, and the mismatch in scales between the oscillatory data and the slowly varying predictions.

TABLE 8.1. *Relative error in microscale inversion for a parameter $m \equiv \theta \in \mathbb{R}$.*

| | HMM | Analytic | Two-stage |
|---------|------------|------------|------------|
| Model A | 0.04563540 | 0.02556686 | 0.02344292 |
| Model B | 0.03623084 | 0.02234864 | 0.06537146 |
| Model C | 0.05210436 | 0.00726006 | 0.05578068 |
| Model D | 0.05093572 | 0.00354686 | 0.15121385 |
| Model E | 0.07446168 | 0.05607627 | 0.01708140 |

TABLE 8.2. *Performance time (in seconds) of microscale inversion for the parameter $\theta \in \mathbb{R}$.*

| | HMM | Analytic | Two-stage |
|---------|-------|----------|-----------|
| Model A | 9.42 | 8.86 | 22.13 |
| Model B | 18.30 | 16.60 | 27.45 |
| Model C | 14.90 | 17.38 | 16.47 |
| Model D | 10.27 | 10.09 | 17.15 |
| Model E | 15.88 | 16.36 | 19.64 |

Table 8.1 shows the relative error in the reconstruction of the a scalar parameter $\theta \in \mathbb{R}$, and Table 8.2 contains a comparison of the performance time using the different forward solvers. The analytic and HMM solver perform similarly for all three microstructure models. The longer performance time using the two-stage solver can be attributed to first stage, where inversion for the unknown matrix coefficient A involves three times as many unknowns as direct inversion.

8.1.1. Variations on the infinite dimensional parameter m

For a given vector of unknowns $\theta \in \mathbb{R}^N$, it is possible to find a corresponding infinite dimensional parameter $m(x)$ that is uniquely determined from the values in θ .



FIG. 8.2. Model C parametrized using a continuous function $m(x)$ with $N=6$ degrees of freedom.

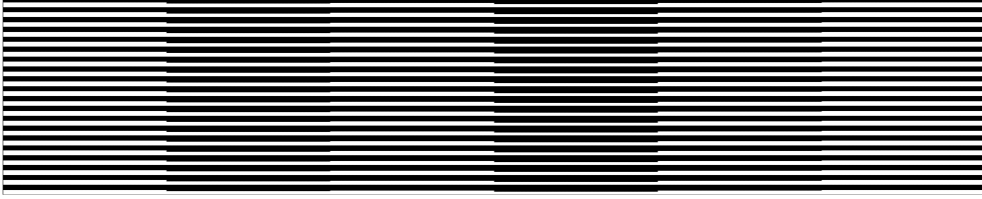


FIG. 8.3. Model B parametrized using a piecewise constant function $m(x)$ with $N=6$.

In one experiment, we let $m(x)$ be a cubic spline interpolant using the values of $\theta \in \mathbb{R}^N$. Predictions are made using HMM “on the fly”. An example of a microstructure with this kind of parametrization is shown in Figure 8.2. Table 8.3 contains the relative errors in the recovered parameter for different values of N . The second parameter

TABLE 8.3. Inversion error in $\theta \in \mathbb{R}^N$ for continuous $m(x)$.

| N | A - Amplitude | B - Area Fraction | C - Angle |
|-----|---------------|-------------------|------------|
| 1 | 0.04237400 | 0.04507309 | 0.05701372 |
| 2 | 0.05485636 | 0.04873258 | 0.04293228 |
| 3 | 0.05552983 | 0.06892129 | 0.06720150 |
| 4 | 0.06572240 | 0.05887249 | 0.05945569 |
| 5 | 0.06691606 | 0.07173517 | 0.08507094 |
| 6 | 0.06761214 | 0.07921053 | 0.09011505 |

TABLE 8.4. Inversion error in $\theta \in \mathbb{R}^N$ for piecewise constant $m(x)$.

| N | A - Amplitude | B - Area Fraction | C - Angle |
|-----|---------------|-------------------|------------|
| 1 | 0.04563540 | 0.02234864 | 0.05210436 |
| 2 | 0.05786556 | 0.02244457 | 0.05886389 |
| 3 | 0.06187033 | 0.04806429 | 0.06601630 |
| 4 | 0.07288481 | 0.07027316 | 0.08523131 |
| 5 | 0.06697655 | 0.09667535 | 0.08324536 |
| 6 | 0.08680081 | 0.07828320 | 0.08282462 |

space for determining the minimizer of (8.1) is the set of piecewise constant functions $m(x)$ (see Figure 8.3 for an example of $m \rightarrow a^\epsilon(m)$ in this case). Forward computations

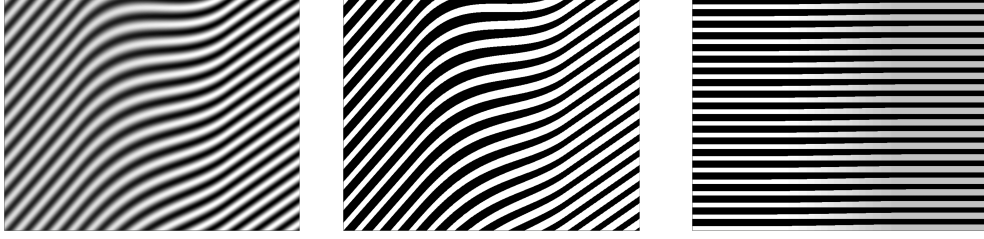


FIG. 8.4. Microstructure models for continuous vector fields $m(x) = (m_1(x), m_2(x))$. Left to right: Amplitude/Angle, Area Fraction/Angle, Amplitude/Area Fraction.

are made using a HMM solver that efficiently makes use of precomputed values of $\hat{A}(m)$. Table 8.4 contains the errors in the recovered parameter for different values of N .

Next, we assume that the unknown parameter m is a vector valued function,

$$m(x) = (m_1(x), \dots, m_M(x)),$$

where M is the number of microscale features to be recovered. The theory developed earlier relates to a scalar parametrization, $M = 1$. For the general problem, each function $m_i(x)$, $1 \leq i \leq M$, is assumed to be a scalar function with N degrees of freedom. Figure 8.4 shows the examples that we use of a coupled parameterization between two different features, $M = 2$.

The microstructure in models A/C, B/C, and A/C, respectively, are represented by the coefficients

$$a_{AC}^\epsilon(m_1, m_2, x) = a_A^\epsilon(m_1, \tilde{x}), \quad \tilde{x} = \sigma_{m_2} x, \quad (8.7)$$

$$a_{BC}^\epsilon(m_1, m_2, x) = .5 + 2\chi_{\{(0, m_1)\}}(\tilde{x}_2), \quad \tilde{x} = \sigma_{m_2} x, \quad (8.8)$$

$$a_{AB}^\epsilon(m_1, m_2, x) = .5 + 2m_1\chi_{\{x_2 < m_2\}}(x). \quad (8.9)$$

Therefore, the inverse problem reduces to determining a finite dimensional vector of unknowns, $\theta \in \mathbb{R}^{MN}$. Taking these ideas further, we perform experiments in the case $M = 2$. Table 8.5 contains the errors from the numerical experiments.

TABLE 8.5. Inversion error in $\theta \in \mathbb{R}^{2N}$ for continuous $m(x) = (m_1(x), m_2(x))$.

| N | Angle/Amplitude | Angle/Area Fraction | Amplitude/Area Fraction |
|-----|-----------------|---------------------|-------------------------|
| 1 | 0.03082785 | 0.04804962 | 0.04394855 |
| 2 | 0.12689231 | 0.07667133 | 0.06829348 |
| 3 | 0.11401958 | 0.09285163 | 0.07980421 |

REMARK 8.1. In certain cases, the solutions to cell problems corresponding to different microscale coefficients a^ϵ are indistinguishable. In particular, for a fixed m , there exists a \tilde{m} such that the homogenized coefficients corresponding to a parametrized area fraction $m \rightarrow a_{VF}^\epsilon(m)$ are equal to the homogenized coefficients corresponding to a parametrized amplitude $\tilde{m} \rightarrow a_{AMP}^\epsilon(\tilde{m})$. However, if the recovered parameter is constrained to a convex subset of the search space, the problem can be reformulated to guarantee a unique recovery.

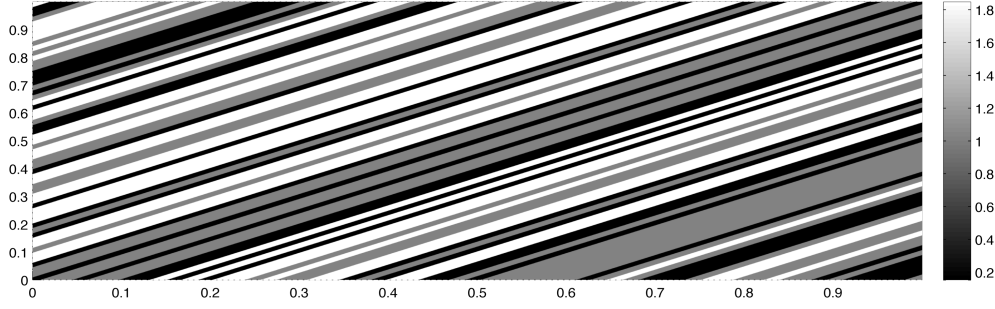


FIG. 8.5. *Random microstructure in layered materials.*

8.1.2. Random microstructure We consider a model of layered media where the microstructure is represented by a random coefficient $m(x) \rightarrow a^\epsilon(m(x), x, \omega)$, where

$$a^\epsilon(m, x, \omega) = a(m, X_\epsilon(x, \omega)), \quad (8.10)$$

$$X_\epsilon(x, \omega) = \sum_{j=0}^{\lfloor 1/\epsilon \rfloor} X_j(\omega) \chi_{[j\epsilon, (j+1)\epsilon)}(\tilde{x}), \quad \tilde{x} = (\sigma_{\pi/4} x)_2, \quad (8.11)$$

where ω is an element of a sample space \mathcal{X} and X_j are independent, random variables that are uniformly distributed on the interval $[-1, 1]$. Figure 8.5 shows a plot of (8.10) for $a(m, \xi) = 1 + m\xi$.

In these experiments, we fix $m \equiv \theta \in (0, 1)$ and the least-squares minimization problem (8.1) is solved for 100 realizations of the coefficient, $a^\epsilon(\theta, \omega)$. In each trial, the same realization is used to generate both the data,

$$y^\epsilon = \mathcal{G}(a^\epsilon)_k = a^\epsilon \nabla u_k^\epsilon \cdot n|_{\partial\Omega},$$

and the predictions, $z = \mathcal{G}(A)_k$.

We compare the performance of HMM forward solvers corresponding to three different choices of the size of the local subdomains I_δ ; $\delta = 2\epsilon$, $\delta = 4\epsilon$, and $\delta = 8\epsilon$. Table 8.6 contains the frequency of recovered parameters from $\hat{\theta}$ lying in an interval E_θ centered at the true parameter. The results are consistent with the expectation that the accuracy of the parameter estimation using HMM would improve with increased cell size.

TABLE 8.6. *Microscale parameter inversion for a random microstructure. The true parameter is $\theta = .8$, and the frequency of recovered parameters $\hat{\theta}$ lying in the interval E_θ is given.*

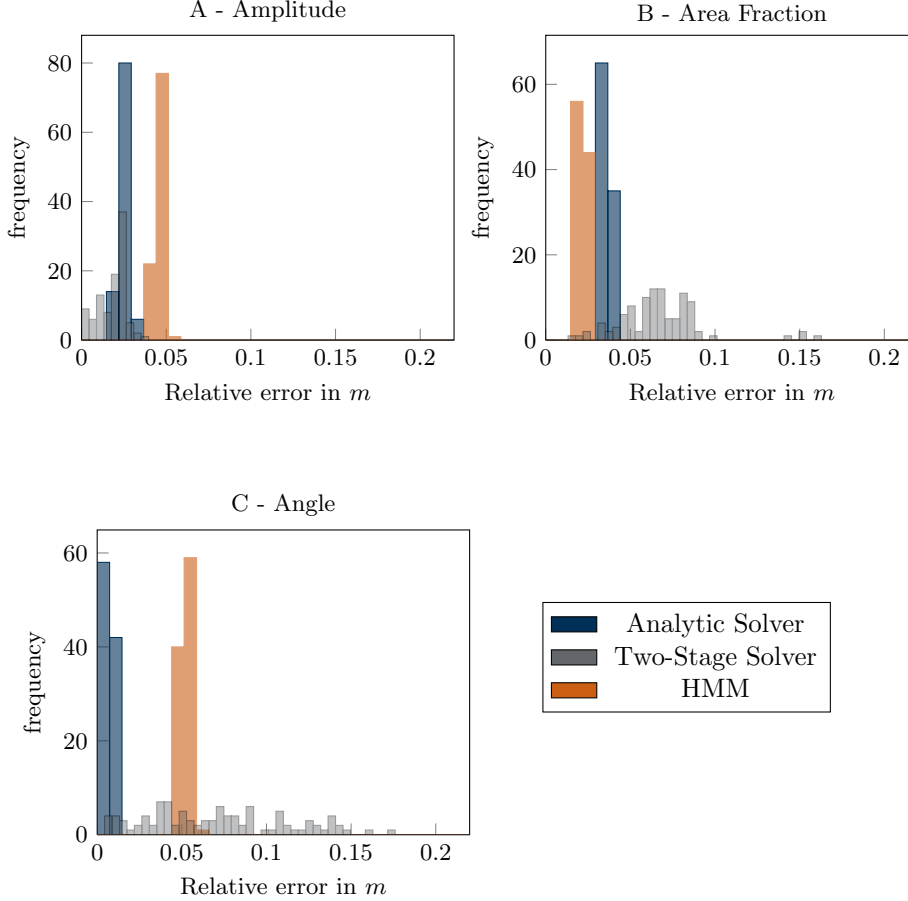
| E_θ | $\delta = 2\epsilon$ | $\delta = 4\epsilon$ | $\delta = 8\epsilon$ |
|--------------|----------------------|----------------------|----------------------|
| $(.7, .9)$ | 16% | 26% | 57% |
| $(.75, .85)$ | 4% | 14% | 29% |
| $(.79, .81)$ | 0% | 2% | 11% |

8.1.3. Noisy data

Here, measurement error is introduced in the observations,

$$y^\epsilon = \mathcal{G}(a^\epsilon)_k (1 + \xi),$$

FIG. 8.6. **Microscale inversion with noisy observations ($N=M=1$).** The histogram shows the results of 100 trials of microscale inversion with measurement error of 10% added to the synthetic data.



where ξ is a normally distributed random variable with mean zero and standard deviation $\sigma = .1$. Figure 8.6 contains histograms of the relative errors in the recovered parameter $m \equiv \theta \in \mathbb{R}$. From the experiments it is clear that the two-stage procedure resulted in errors with a larger variance than the errors from direct inversion. This indicates that the procedure is less robust to noisy input data.

8.2. Medical imaging ($b^e > 0$) The modeling of wave propagation in heterogeneous media is an important problem in many areas of science and engineering. Current approaches attempt to design methods that account for variations in material microstructures when solving equations of motion in an effective medium [12]. Diffusion in random heterogeneous media is studied in [13, 16].

We will consider a medical imaging technique that uses a combination of optical and ultrasonic waves to determine properties of a medium from surface measurements. In quantitative Photoacoustic Tomography, (qPAT), optical coefficients are reconstructed from knowledge of the absorbed radiation map [4, 5].

Let $\Omega \subset \mathbb{R}^2$ represent a medium of interest and $\Lambda \subset \mathbb{R}_+$ a set of wavelengths in-

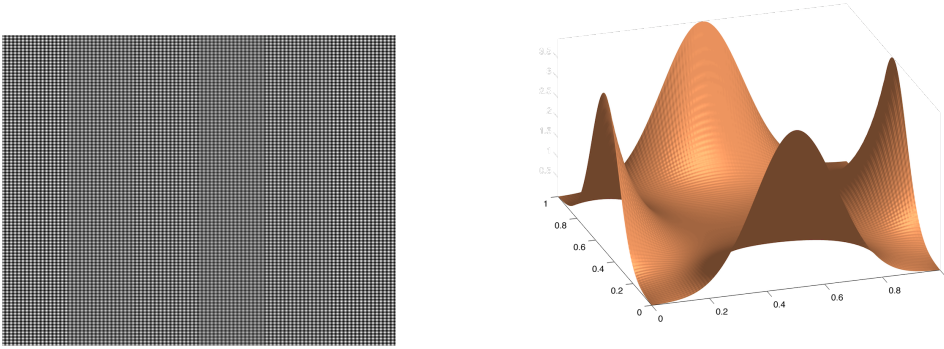


FIG. 8.7. *Left: microscale coefficient $a_D^\epsilon(m(x), x)$. Right: solution to qPAT model (8.12) corresponding to four sources on the boundary.*

cluded in the experiment. The density of photons at wavelength λ , denoted by $u(x, \lambda)$, solves the second-order elliptic equation

$$\begin{cases} -\nabla \cdot (a(x, \lambda) \nabla u(x, \lambda)) + \sigma(x, \lambda) u(x, \lambda) = 0 & x \in \Omega \\ u(x, \lambda) = g(x, \lambda) & x \in \partial\Omega. \end{cases} \quad (8.12)$$

Here, a and σ are diffusion and absorption coefficients that are dependent on the wavelength λ . The ultrasound generated by the absorbed radiation is quantified by the Grüneisen coefficient, $\Gamma(x, \lambda)$. The objective of qPAT is to recover (a, σ, Γ) using the measured data from photoacoustic experiments corresponding to an illumination pattern $g(x, \lambda)$.

We will modify the numerical examples from [5] by considering the forward model (8.12) with diffusion coefficients that have variations on multiple spatial scales, $a = a^\epsilon$. For simplicity, we will assume that the absorption, diffusion, and Grüneisen coefficients can be expressed as

$$\sigma(x, \lambda) = \sum_{i=1}^2 \beta_i(\lambda) \sigma_i(x), \quad a^\epsilon(x, \lambda) = \alpha(\lambda) a^\epsilon(x), \quad \Gamma(x, \lambda) = \Gamma(x).$$

The measured data takes the form

$$\mathcal{G}(a, u = G(a)) = \Gamma(x, \lambda) \sigma(x, \lambda) u(x, \lambda), \quad x \in \Omega, \quad \lambda \in \Lambda. \quad (8.13)$$

In the numerical experiments, the measured data (8.13) involves the solutions to (8.12) for each wavelength in the set $\Lambda = \{.2, .3, .4\}$. Four illuminations are used for each wavelength. The wavelength dependent components of the coefficients are set to be

$$\beta_1(\lambda) = \frac{\lambda}{\lambda_0}, \quad \beta_2(\lambda) = \frac{\lambda_0}{\lambda}, \quad \alpha(\lambda) = (\lambda/\lambda_0)^{3/2},$$

where the wavelength $\lambda_0 = .3$ normalizes the amplitude of the coefficients. The spatial components of the coefficients are given as

$$\begin{aligned} \Gamma(x) &= .8 + .4 \tanh(4x - 4), \\ \sigma_1(x) &= .2 - .1e^{-2\pi|x-x_0|^2}, \quad \sigma_2(x) = .2 + .1e^{-2\pi|x-x_0|^2}, \quad x_0 = (.5, .5). \end{aligned}$$

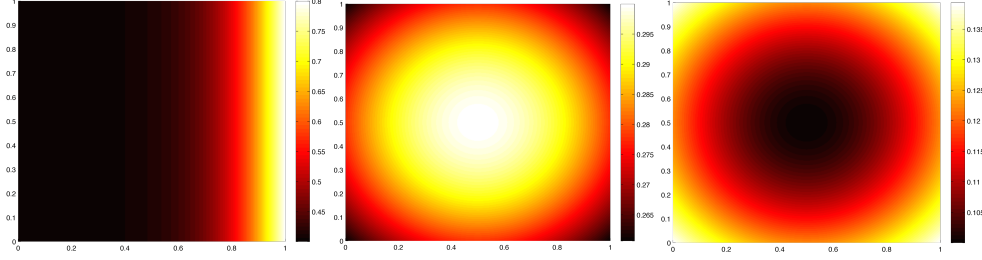


FIG. 8.8. **Spatial components of the qPAT model.** *Left to right: Grüneisen coefficient $\Gamma(x)$, and absorption component functions $\sigma_1(x)$ and $\sigma_2(x)$.*

Figure 8.8 contains plots of the spatial components of Γ and σ .

The microstructure in models D and E, respectively, are represented by the coefficients

$$a_D^\epsilon(m(x), x) = a_A^\epsilon(m(x_1), x_1) a_A^\epsilon(m(x_2), x_2), \quad (8.14)$$

$$a_E^\epsilon(m(x), x) = .5 + 2\chi_{\{[0, m] \times [0, m]\}}(x). \quad (8.15)$$

$$(8.16)$$

As in [5], the reconstruction errors are given for synthetic data with no noise added. However, errors are introduced from averaging the multiscale solution and projection onto the coarse grid. The results in Table 8.7 show inversion results using a HMM forward solver for macroscopic predictions. Here the parameters are chosen to be $\epsilon = 1/100$, $H = 1/20$, $\delta = 3\epsilon$, and $h = 1/800$. The vector of unknowns, $\theta \in \mathbb{R}^N$ determines a piecewise constant function $m(x)$.

TABLE 8.7. *Inversion errors for parameter estimation in qPAT models containing periodic cell structures.*

| N | D - Amplitude | E - Area Fraction |
|-----|---------------|-------------------|
| 1 | 0.05605865 | 0.01529364 |
| 2 | 0.07461357 | 0.01838472 |
| 3 | 0.07146362 | 0.02986680 |
| 4 | 0.08319615 | 0.03748564 |
| 5 | 0.13636728 | 0.04616734 |
| 6 | 0.08914877 | 0.03729032 |

8.3. Seismic waveform inversion ($b^\epsilon < 0$)

In exploration geophysics, scientists attempt to determine the geological properties of the Earth's crust that govern the propagation of acoustic waves (see [24] for an overview). In full waveform inversion, the goal is to find a subsurface model that produces the best fit to reflection data recorded from seismic surveys. Each prediction is simulated using the physics of the experiment. This corresponds to an inverse problem for partial differential equations where the unknown coefficients represent properties of the sedimentary layers, e.g. velocities, porosity, and saturation.

Full waveform inversion is the result of combining numerical methods for the simulation of wave propagation with optimization techniques to minimize the data misfit

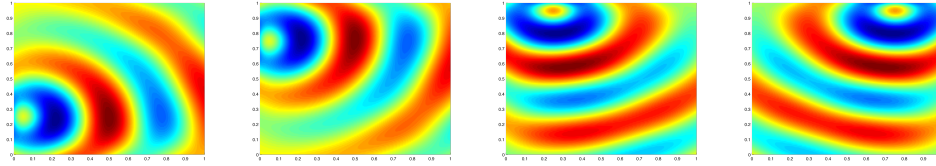


FIG. 8.9. Solutions of the multiscale Helmholtz equation (8.17) for wavelength $\omega=4\pi$ and multiscale coefficient $a=a_A^\epsilon$.

term (see [11] for a discussion of multiscale full waveform inversion). Traditional finite element methods (FEM) or finite difference methods (FDM) for wave propagation in the high frequency regime come with a considerably high computational cost due to the highly oscillatory nature of the propagating waves [14].

The forward problem can be modeled in both the time domain and the frequency domain. In theory, both approaches are equivalent, however the choice of model can influence the design of specific numerical methods to optimize performance. An advantage of the frequency domain model is that a coarse discretization of the frequencies can be used to produce images that are free from aliasing [3, 18, 22].

A major hurdle in full waveform inversion is the presence of local minima in the least-squares functional for the data misfit. In [21], adjoint-state methods are used to efficiently calculate the gradient of the least-squares functional and speed up the optimization. We emphasize that in this work we use standard optimization routines in order to fully study the effects of fitting an effective model to the data.

Our numerical examples correspond to problems that mimic the models used in seismic waveform inversion. Here, the model parameters represent the spatially varying area fraction, angle, and amplitude of the layers. The forward model G maps a to the solution to the 2D variable coefficient Helmholtz equation on the square $\Omega=[0,1]^2$,

$$\nabla \cdot (a(x) \nabla u) + \omega^2 u(x) = \delta(x - x_s) \quad x \in \Omega, \quad (8.17)$$

where a is the model parameter that characterizes the density of the medium, ω is the wave number, and u is the spatially varying pressure field arising from a disturbance at a source located at $x_s \in \Omega$. We impose the absorbing boundary condition

$$a \nabla u \cdot n - iku = 0 \quad \text{on } \partial\Omega, \quad (8.18)$$

where $k=a^{-1/2}\omega$. The seismic data is represented as the collections of solutions measured on the sensor domain, $\mathcal{G}(a, u=G(a))=l_j(u|_D)$ (see Figure 8.9).

In the numerical simulations, the wavelength is $\omega=4\pi$ and the Dirichlet data is obtained from solutions corresponding to multiple sources at $x_{s_1}=(0,.25)$, $x_{s_2}=(0,.75)$, $x_{s_3}=(.25,1)$, and $x_{s_4}=(.75,1)$. Results shown in Table 8.8 demonstrate microscale inversion of the Helmholtz equation (8.17) using the methods described earlier. Here the parameters are chosen to be $\epsilon=1/120$, $H=1/40$ and $h=1/800$, $\delta=6\epsilon$.

9. Conclusion

We present computational techniques for solving inverse problems for multiscale partial differential equations. Our goal is to recover microscale information from PDE constrained optimization. Instead of directly working with the effective equation we

TABLE 8.8. *Inversion error for parameter estimation in the Helmholtz model.*

| N | A - Amplitude | B - Area Fraction | C - Angle |
|-----|---------------|-------------------|------------|
| 1 | 0.02776429 | 0.03736824 | 0.03891544 |
| 2 | 0.04400273 | 0.02612802 | 0.07489835 |
| 3 | 0.04607522 | 0.01553997 | 0.06326932 |
| 4 | 0.07915712 | 0.00976197 | 0.25927552 |
| 5 | 0.05350197 | 0.01566102 | 0.17280984 |
| 6 | 0.04874272 | 0.01968874 | 0.21757778 |

constrain the search space by representing the microscale by a limited number of parameters in order to have a well-posed inverse problem. When a parameter based effective model exists we use that, otherwise, the numerical heterogeneous multiscale method (HMM) can be used even when the explicit form of the effective equation is not known. By applying recovery results for inverse conductivity problems with special anisotropy [2], we can prove that certain microstructure features can be determined uniquely from the Dirichlet to Neumann map corresponding to the effective equations. We provide numerical examples, which show quantitative convergence information with respect to numerical resolution, scale separation and parameterization strategies. We also provide numerical results that demonstrate the performance of these techniques applied to random media and simple models with lower order terms of the form used in medical imaging and exploration seismology.

The goal of the current research has been a proof of concept and there are natural future directions outside the scope of the current paper. For example, in more realistic applications where higher resolution of $m(x)$ is required, other minimization techniques must be used. Good candidates would be adjoint-state based methods, which are used in full waveform inversion [21]. Another direction is to further probe random cases and explore the use of multiple parameters $m(x)$ in connection to known prior information in specific applications.

Acknowledgements. This work has benefited from valuable discussions with Assyr Abdulle, Kui Ren, Pingbing Ming and Fenyang Tang. This research was supported in part by NSF grant DMS-1217203, the Texas Consortium for Computational Seismology, and Institut Mittag-Leffler. CF was also supported in part by NSF grant DMS-1317015.

REFERENCES

- [1] Giovanni Alessandrini. Open issues of stability for the Inverse Conductivity Problem. *Journal Inverse Ill-Posed Problems*, 15(2006014115):1–10, 2007.
- [2] Giovanni Alessandrini and Romina Gaburro. Determining conductivity with special anisotropy by boundary measurements. *SIAM Journal on Mathematical Analysis*, 33(1):153–171, 2001.
- [3] Guido Baeten, Jan Willem de Maag, René-Edouard Plessix, Rini Klaassen, Tahira Qureshi, Maren Kleemeyer, Fons ten Kroode, and Zhang Rujie. The use of low frequencies in a full-waveform inversion and impedance inversion land seismic case study. *Geophysical Prospecting*, 61(4):701–711, July 2013.
- [4] Guillaume Bal and Kui Ren. Multi-source quantitative PAT in diffusive regime. *Inverse Problems*, 27:1–24, 2011.
- [5] Guillaume Bal and Kui Ren. On multi-spectral quantitative photoacoustic tomography in diffusive regime. *Inverse Problems*, 28(2):025010, February 2012.
- [6] Alain Bensoussan, Jacques Louis Lions, and George Papanicolaou. *Asymptotic Analysis for*

- Periodic Structures*, volume 5 of *Studies in Mathematics and its Applications*. North-Holland Pub. Co.(Amsterdam and New York and New York), 1978.
- [7] Liliana Borcea. Electrical impedance tomography. *Inverse Problems*, 18(6):R99–R136, December 2002.
 - [8] Alberto P. Calderón. On an inverse boundary value problem. *Computational & Applied Mathematics*, 25(2-3):133–138, 2006.
 - [9] Margaret Cheney, David Isaacson, and Jonathan C. Newell. Electrical Impedance Tomography. *SIAM Review*, 41(1):85–101, January 1999.
 - [10] Weinan E and Björn Engquist. The heterogenous multiscale methods. *Communications in Mathematical Sciences*, 1(1):87–132, March 2003.
 - [11] A. Fichtner, J. Trampert, P. Cupillard, E. Saygin, T. Taymaz, Y. Capdeville, and A. Villasenor. Multiscale full waveform inversion. *Geophysical Journal International*, 194(1):534–556, April 2013.
 - [12] Jacob Fish, Vasilina Filonova, and Sergey Kuznetsov. Micro-inertia effects in nonlinear heterogeneous media. *International Journal for Numerical Methods in Engineering*, 91(13):1406–1426, September 2012.
 - [13] Baskar Ganapathysubramanian and Nicholas Zabaras. Modeling diffusion in random heterogeneous media: Data-driven models, stochastic collocation and the variational multiscale method. *Journal of Computational Physics*, 226(1):326–353, September 2007.
 - [14] Frank Ihlenburg and I Babuška. Solution of Helmholtz problems by knowledge-based FEM. *Computer Assisted Mechanics and Engineering Sciences*, (2):397–415, 1997.
 - [15] V. V. Jikov, S. M. Kozlov, and O. A. Oleinik. *Homogenization of Differential Operators and Integral Functionals*. Springer, 2011.
 - [16] Babak Kouchmeshky and Nicholas Zabaras. The effect of multiple sources of uncertainty on the convex hull of material properties of polycrystals. *Computational Materials Science*, 47(2):342–352, December 2009.
 - [17] Pingbing Ming and Pingwen Zhang. Analysis of the Heterogeneous Multiscale Method for Elliptic Homogenization Problems. *Journal of the American Mathematical Society*, 18(1):121–156, 2005.
 - [18] W.A. Mulder and R.-E. Plessix. Exploring some issues in acoustic full waveform inversion. *Geophysical Prospecting*, 56(6):827–841, November 2008.
 - [19] G Pavliotis and A Stuart. *Multiscale Methods: Averaging and Homogenization*, volume 53. Springer, 2008.
 - [20] G.A. Pavliotis, A.M. Stuart, and J. Nolen. Multiscale modelling and inverse problems. In Robert Graham, Ivan G. and Hou, Thomas Y. and Lakkis, Omar and Scheichl, editor, *Numerical Analysis of Multiscale Problems*, pages 1–34. Springer Berlin Heidelberg, 2012.
 - [21] R.-E. Plessix. A review of the adjoint-state method for computing the gradient of a functional with geophysical applications. *Geophysical Journal International*, 167(2):495–503, November 2006.
 - [22] Laurent Sirgue and R. Gerhard Pratt. Efficient waveform inversion and imaging: A strategy for selecting temporal frequencies. *GEOPHYSICS*, 69(1):231–248, January 2004.
 - [23] J Sylvester. An anisotropic inverse boundary value problem. *Communications on Pure and Applied Mathematics*, 2(43):201–232, 1990.
 - [24] W W Symes. The seismic reflection inverse problem. *Inverse Problems*, 25(12), December 2009.
 - [25] Gunther Uhlmann. The Dirichlet to Neumann Map and Inverse Problems. Technical report.
 - [26] Gunther Uhlmann. Commentary on Calderóns paper 28 , On an Inverse Boundary Value Problem. *Selected papers of Alberto P. Calderón*, pages 1–12, 2008.